1991ApJ...371..684B

THE ASTROPHYSICAL JOURNAL, 371:684–695, 1991 April 20

ENHANCED WINDS AND TIDAL STREAMS IN MASSIVE X-RAY BINARIES

JOHN M. BLONDIN
Department of Astronomy, University of Virginia, Charlottesville, VA 22903
AND
IAN R. STEVENS[1] AND TIMOTHY R. KALLMAN
Laboratory for High Energy Astrophysics, NASA/Goddard Space Flight Center, Greenbelt, MD 20771
Received 1990 August 20; accepted 1990 October 2

ABSTRACT

The tidal effects created by the presence of a compact companion are expected to induce a stream of enhanced wind from the early-type primary star in massive X-ray binary systems. In this paper we present two-dimensional gasdynamical simulations of such streams. We find that the wind enhancement is a sensitive function of the binary separation, and develops into a tidal stream as the primary approaches its critical surface. For typical system parameters, the Coriolis force deflects the stream sufficiently that it does not impact directly on the compact companion but passes behind it. The density in the stream can reach values of 20–30 times the ambient wind density, leading to strong attenuation of the X-ray flux that passes through the tidal stream, providing a possible explanation of the enhanced absorption events seen at later phases in the X-ray observations of massive X-ray binary systems such as Vela X-1. In contrast to the time-variable accretion wake, the tidal stream is relatively stationary, producing absorption features that should remain fixed from orbit to orbit. For systems with a strong tidal stream, the large asymmetry in the accreting wind results in the accretion of angular momentum of constant sign, as opposed to systems without streams, where the sign of the accreted angular momentum can change.

Subject headings: hydrodynamics — stars: winds — X-rays: binaries

1. INTRODUCTION

Massive X-ray binaries (hereafter MXRBs) consist of an OB-type giant or supergiant primary star with a strong stellar wind, in close orbit with an accreting compact secondary (either a neutron star or a black hole). As such, MXRBs provide a very useful laboratory for the study of a range of energetic astrophysical phenomena, such as the physics of neutron stars, stellar evolution, binary tidal interactions, accretion flows, and the structure of stellar winds. The X-rays from the neutron star provide an active probe of the stellar wind of the primary, altering the ionization and thermal structure of the wind material and consequently changing the wind dynamics. In turn, the observed X-ray spectrum and the attenuation inferred from it, can provide information about the temporal behavior of MXRB systems.

In most MXRB systems the primary star is thought to be close to filling its Roche lobe (see Conti 1978 for a review of the observational data). In this case, the shape of the primary star will be distorted by the binary gravitational potential, and, in particular the primary will be extended in the general direction of the inner Lagrangian point. This means that the stellar wind will start farther from the center of the primary and will be "fighting" less gravity in the direction of the inner Lagrangian point, resulting in an enhanced mass loss from the primary along the line of centers of the system (Friend & Castor 1982). In the limit that the atmosphere of the primary reaches all the way to the Roche surface the stellar wind along the line of centers will be replaced by "Roche lobe overflow" (RLOF). Which mode of mass transfer dominates will depend on the precise system parameters. In systems such as Cen X-3 and SMC X-1, even though the primary stars will have their own intrinsic stellar winds (the primary stars in these two systems being respectively of types O6.5 III, and B0 I), the primary mode of mass transfer is believed to be via RLOF, and an accretion disk is believed to be present around the compact star (Petterson 1978). The neutron star pulse period and the spin history of these systems also support the inference of the presence of an accretion disk (Joss & Rappaport 1984). However, in systems such as Vela X-1 and 4U 1700−37 the accretion is believed to be wind-dominated (Conti 1978). Even in these systems, because the derived stellar parameters suggest that the primary star is still close to filling its Roche lobe, a tidal stream of enhanced mass loss in the direction of the compact star may be present, even though the dominant mass-loss mechanism is the stellar wind of the primary.

The presence of a tidal stream will have potentially major consequences on the mass accretion rate onto the neutron star and on the attenuation of X-rays from the neutron star. If the gas stream approaches sufficiently close to the compact companion, it will be accreted in whole or in part, substantially increasing the total mass accretion rate. This in turn will increase the accretion-driven X-ray luminosity above that expected for spherically symmetric stellar wind accretion (cf. Friend & Castor 1982). Separate from this increase in X-ray luminosity the gas stream will provide a source of strong attenuation of the X-rays, whether or not the stream impinges on the neutron star (Petterson 1978). This attenuation will manifest itself in orbital-phase–dependent absorption of the soft X-rays from the neutron star (Haberl, White, & Kallman 1989). It is these two observational consequences that provide the motivation for seeking to include such tidal effects in MXRB models.

The observational evidence for gas streams in MXRBs rests

---

[1] NAS/NRC Research Associate.

primarily with the phase-dependent X-ray attenuation. Episodic enhancements in the absorption of X-rays (as inferred from an increase in the X-ray hardness ratio, or from line-profile variations) have been well documented in several MXRB systems, in particular Vela X-1 (Kallman & White 1982) and 4U 1700−37 (Fahlman & Walker 1980; Haberl et al. 1989). Haberl et al. (1989) modeled the absorption data of 4U 1700−37 by assuming a stream of material arising from the primary star with roughly 10 times the density of the ambient wind. However, other interpretations for the enhanced absorption have been proposed. Eadie et al. (1975) interpreted the absorption dips in the *Ariel 5* Sky Survey observations of Vela X-1 as indicative of attenuation near to shock fronts in an accretion wake around the neutron star. Alternatively, Fransson & Fabian (1980) suggested that the photoionization of the stellar wind could result in a wake of swept-up, stagnant wind trailing the X-ray source in orbit, contributing to the X-ray absorption at late phases.

Friend & Castor (1982), using a modified Castor, Abbott, & Klein (1975, hereafter CAK) wind model, have calculated models of MXRBs including tidal effects on the primary stellar surface. These models did indeed show an enhanced stream of mass loss in the direction of the neutron star, though the level of the density enhancement was much less than that derived by Haberl et al. (1989), typically less than a factor of 2. However, Stevens (1988), in his model of the highly eccentric binary X-ray transient *Ariel* 0538−66, showed that under certain circumstances extremely dense streams of material from the primary could result from tidal interactions with a neutron star companion.

In this paper, which is a follow-up to Blondin et al. (1990, hereafter Paper I), we present results of two-dimensional gasdynamics calculations for the stellar wind in MXRBs which take into account tidal departures from sphericity in the primary. The simulations presented in Paper I provided evidence for the strong variability of the accreting stellar wind, the importance of Compton heating and cooling, and the rapid changes in the sign of the accreted angular momentum. They also illustrated how the anomalous X-ray absorption at late orbital phases could be explained by dense filaments in the accretion wake or in the photoionization wake. However, no attempt was made to include the distortion of the primary by the binary potential, and hence no comment could be made on the possibility that this absorption is produced by a tidal stream rather than an accretion wake. In an effort to identify the source of the phase-dependent absorption, and to understand quantitatively the effects of a tidal stream on the mass accretion rate, we have extended the numerical models of Paper I to include the tidal enhancement of the stellar wind and the formation of a gas stream.

The question of whether the primary star corotates with the orbit of the neutron star companion is a potentially important factor in the formation of a tidal bulge and stream, as is whether the orbit is circular or eccentric. However, for the time being we concentrate on the better defined problem of corotating systems; the case of noncorotation will be briefly considered in § 4.2. We will also limit ourselves to circular systems, and will not deal with highly eccentric orbits as inferred in GX 301−2 and A0538−66. Section 2 presents the improvements made in the model over that of Paper I. The results for the wind structure and its effect on the mass accretion rate and X-ray attenuation, allowing for Roche geometry, are presented in § 3. In § 4 we discuss the results of these models in relation to the observed properties of MXRBs, and conclude with a brief summary in § 5.

2. MODEL IMPROVEMENTS

The numerical model used in the simulations presented here is essentially the same as that used in Paper I, but with the boundary condition at the surface of the primary modified to account for tidal distortions caused by the presence of the compact companion. In addition, more attention was given to the modeling of the subsonic region of the stellar wind to ensure a reasonable dependence of the wind properties on the stellar radius and surface potential. We will review the salient features of the model here and refer the reader to Paper I for a more complete description of the calculation.

We use a two-dimensional, time-dependent gasdynamics code to calculate the flow of a stellar wind in the equatorial plane of a close binary system. The numerical grid is centered on the center of mass of the system, and is rotated at the angular frequency of the orbiting system. The zone volume increases radially as $r^2\,dr$ to provide the correct $1/r^2$ divergence of the density in a constant-velocity wind, neglecting the small displacement of the center of mass and the center of the primary. We assume no flow in or out of the plane of the grid, and thereby ignore any gravitational focusing of the wind in the third dimension. The numerical scheme is based on the direct Eulerian version of the piecewise parabolic method developed by Collela & Woodward (1984). This code has been used to study axisymmetric (Fryxell, Taam, & McMillan 1987) and asymmetric (e.g., Fryxell & Taam 1988) accretion onto compact objects, as well as to study the large-scale gas flow in MXRBs (Paper I). In addition to the usual gravitational and fictitious (i.e., Coriolis and centrifugal) forces, we include the radiation force of the flux from the primary star that is responsible for driving the stellar wind. Both the gravitational force and the radiation force of the primary are calculated only along the radial direction of the grid. The large mass difference in this system leads to only a small displacement of the centers of the grid and primary. This approximation therefore produces an error of less than 6% in angle at the largest angles in the grid, while the error is identically zero along the line of centers, where we are most concerned with the flow dynamics. We follow the line-driven wind model of CAK and use the Sobolev approximation to calculate the line force exerted on the wind material. We include the finite-disk correction factor in the line force, which produces mass-loss rates and terminal velocities in better agreement with observed O star winds (Friend & Abbott 1986; Pauldrach, Puls, & Kudritzki 1986). Although this correction term was derived for a spherical primary, the difference caused by the distorted surface is relatively small compared with the assumption of a point source for the primary. The code is written to include heating due to the X-rays from the neutron star (assuming a 10 keV bremsstrahlung spectrum) and cooling due to the X-rays and the locally emitted radiation, all in the optically thin limit. In Paper I we accounted for the X-ray photoionization of the wind by cutting off the wind-driving force when the local ionization parameter, $\xi = 4\pi F_x/n$ (F_x is the local X-ray flux, and n is the number density of the wind), exceeded some critical value, $\xi_{\rm cr}$. Both the heating and cooling and the photoionization cutoff are removed in the first set of simulations reported here (§ 3.1), so that there exists a continuously accelerated, adiabatic stellar wind. We limit the gas temperature to a minimum value equal to the effective temperature of the primary such that the wind behaves isothermally at large radii where adiabatic expansion would have cooled the wind to very low temperatures. We then present a full simulation in which the complete code of Paper I along with the modifications of this paper are included (§ 3.2).

Before running the two-dimensional simulations, we ran extensive tests to verify the ability of the code to model a radiatively driven stellar wind from a subsonic photosphere to a highly supersonic wind approaching the correct terminal velocity, v_∞, and mass-loss rate, $\dot{M}_w$. It was found that the only way to obtain boundary conditions that produced a reasonable, stable stellar wind was to set the values of the velocity and density to constants, v_0 and ρ_0, at the stellar surface. In Paper I the values of v_0 and ρ_0 were largely ignored, as long as the wind remained steady, with $\dot{M}_w$ and v_∞ similar to the values produced by the CAK model. In the present paper, however, our goal is to model the dependence of the stellar wind on the stellar radius and the effective gravitational potential. We must therefore be able to model the stellar wind accurately from the photosphere (highly subsonic), through the sonic point, and up to the terminal velocity.

While the downstream stellar wind is largely insensitive to the value of v_0, we have chosen to set $v_0 = 0$ as a realistic value at the base of the wind. The final steady state wind is virtually independent of v_0, provided that v_0 is much less than the sound speed in the wind. The steady state wind is only slightly sensitive to the value of ρ_0, with a higher ρ_0 producing a larger mass-loss rate and a slower wind. Choosing the correct ρ_0 is the analog of requiring the electron-scattering optical depth of the wind from R_* to infinity to equal unity in the CAK steady state wind models. It is not possible to provide sufficient spatial resolution near R_* in our time-dependent simulations to calculate τ_e for this purpose, so we must find the correct ρ_0 by some other means. By choosing values of ρ_0 to produce wind profiles similar to the CAK solutions, we found that there exists a unique ρ_0 for which the radial velocity in the first zone is equal (or nearly so) to zero. For larger values of ρ_0 the velocity in the first zone is negative. Although this large-ρ_0 solution is not necessarily physical, the wind solution beyond the first few zones appears perfectly reasonable. At lower values of ρ_0 the velocity in the first zone becomes larger, eventually becoming supersonic. The effect of varying ρ_0 is thus to move the sonic point with respect to the stellar surface, again in analogy with the CAK method of fixing $\tau_e = 1$. For the isolated stellar wind, the steady state solution obtained by using this "critical density" conforms quite closely to the CAK solution, with $\dot{M}_w$ and v_∞ differing by no more than a few percent from the CAK values.

For the purposes of the present paper we have modified the shape of the stellar surface at which the stellar wind boundary conditions are applied, to allow for the distortion of the star by the binary gravitational potential. In the absence of any gas flow within the star, the isobaric and isopycnic surfaces will coincide with surfaces of constant effective potential (see, e.g., Tassoul 1978, § 7.2). However, both the distortion of the star and the enhanced mass loss along the line of centers will impose large-scale mass flows within the atmosphere of the primary (Tassoul 1978; Lubow & Shu 1975). In the present problem, where the mass loss is dominated by a radiatively driven wind, we expect these atmospheric currents to be considerably smaller than the mass motions flowing perpendicular to the equipotential surfaces, feeding the radiatively driven stellar wind. Thus, we shall adopt the barotropic condition at the base of the stellar wind, and assume that the density and pressure on the inner boundary of our grid follow a contour of constant effective potential. If the mass loss becomes dominated by RLOF, the horizontal currents induced in the photosphere may become more important, in which case this boundary condition may not be sufficient to describe the mass loss. We note that this boundary condition is not the same as that imposed by Friend & Castor (1982), who calculated a steady state wind by requiring $\tau_e = 1$ at each angle. While their technique appears reasonable in the context of the stellar wind, it seems rather ad hoc in the context of the photosphere of the primary. On the other hand, our assumption is not valid in the presence of large mass flows, which will certainly occur in a mass-losing star. Because of the insensitivity of the wind to these boundary conditions, however, we do not expect much of a difference between our results and those of Friend & Castor (1982).

For a corotating system of mass ratio $q_m = M_x/M_*$, where M_* and M_x are the respective masses of the primary star and the compact X-ray source, the effective binary potential is given by (Kruszewski 1963; Friend & Castor 1982)

$$\Psi_{\rm eff}(r, \theta) = -\frac{GM_*}{r}\left\{1 + \frac{q_m}{[1 + (D/r)^2 - 2(D/r)\cos\theta]^{1/2}} - q_m\left(\frac{r}{D}\right)^2 \cos\theta + \frac{1 + q_m}{2}\left(\frac{r}{D}\right)^3\right\}, \quad (1)$$

where r is the distance from the center of the primary, θ is the angle from the line of centers in the orbital plane, and D is the binary separation. We have ignored the decrease in the gravitational potential due to luminosities approaching their respective Eddington limits (cf. Friend & Castor 1982). In practice we map a surface of constant potential onto our spherical grid so that the boundary conditions imposed at the stellar surface (ρ_0 and v_0) now correspond to this mapped surface rather than the edge of the (spherical) numerical grid. Unfortunately, this distorted surface cannot be mapped onto a spherical grid with infinite accuracy, and the small zone-to-zone differences in the potential at the stellar surface will lead to slight density variations in the downstream wind. To minimize these errors, we used a high-resolution grid near the surface of the primary, with $\Delta R = 0.002 R_*$. Beyond the maximum height of the equatorial bulge, the zone size was increased by 3% per zone to increase the spatial domain of the grid. A similar decrease in zone width was applied near the compact object.

When the primary star is *not* corotating, the problem becomes much more difficult, for the tidal bulge becomes a dynamic wave traveling across the surface of the star rather than a static bulge sitting at a fixed position on the rotating star. We have not attempted to model noncorotating systems in this paper, and will only briefly discuss them in § 4.

The boundary conditions at the compact star were treated the same as in Paper I for the high-resolution runs described in § 3.2. For the series of simulations with varying binary separation we limited the resolution at the neutron star in order to prevent the Courant time step from becoming very small, and thereby making the runs too costly. For these runs we simply removed all the mass, momentum, and energy from the one zone at the location of the compact object. Although this results in only very crude resolution of the accretion dynamics, it still allows the resolution of a standoff bow shock, and the calculated accretion rate agrees quite well with the Bondi-

Hoyle (1944) estimate for axisymmetric accretion (see § 3.1). A comparison of Figures 1*c* and 5 shows the loss of detail within the accretion bow shock by this technique, yet the gas stream remains sufficiently resolved in the small grid runs for our purposes. The other boundary conditions are the same as those in Paper I.

3. RESULTS

3.1. *Stream Dependence on Separation*

To illustrate the emergence of a gas stream as the compact star approaches the surface of the primary, we computed a series of five simulations with different binary separations. We use a primary mass of $M_* = 22\ M_\odot$, a neutron star mass of $M_x = 1.4\ M_\odot$, and a primary radius of $R_* = 2.45 \times 10^{12}$ cm. These models were run on a grid of 185×140 zones, with only limited spatial resolution in the vicinity of the accreting compact object ($\Delta R = 0.008 R_*$). This allows only $\sim$6–8 zones across a typical accretion radius, insufficient to resolve the dynamics of the accretion process. In Figures 1*a*–1*d*, density plots are shown for four of these simulations at a time $t = 4 \times 10^5$ s, sufficiently late in the evolution that the stellar wind has reached a steady state. In these models the gravity of the compact star has been included, but for the time being we have assumed an adiabatic wind (albeit with a minimum temperature equal to the effective temperature of the primary) and have not included X-ray ionization effects (cf. Paper I).

This series illustrates both the gradual enhancement of the wind into a gas stream and the growing complexity in the accretion wake as it interacts with this stream. For the most widely separated model shown in Figure 1, with $D/R_* = 1.70$, tidal effects are seen to be minimal, and the only structure of note is that of the accretion wake around the neutron star. The tidal deviation of the stellar surface is limited to less than 3% of the stellar radius. The downstream wind is only slightly enhanced by the gravitational effects, and the accretion wake appears undisturbed. In contrast, the tidal effects are dramatic for the model with the two stars closest together with $D/R_* = 1.57$, an approximately 10% decrease in the binary separation. In this case a dense stream of material leaves the primary surface along the line of centers. The density in the center of the stream is typically 20–30 times larger than the density of the undisturbed wind at the same distance from the primary. After being dragged behind in orbit by the Coriolis force, the stream is deflected toward the compact object by its gravitational potential, and eventually strikes the accretion wake downstream of the compact object.

The structure of the accretion wake becomes more complicated as the strength of the gas stream increases. This is a direct result of an increasing asymmetry in the stellar wind approaching the compact object. As the wind approaching on the stream side becomes denser and slower, there is a gradual increase in the asymmetry of the accreted angular momentum. This leads to an oscillation of the bow shock or tail shock[2] (see, e.g.,

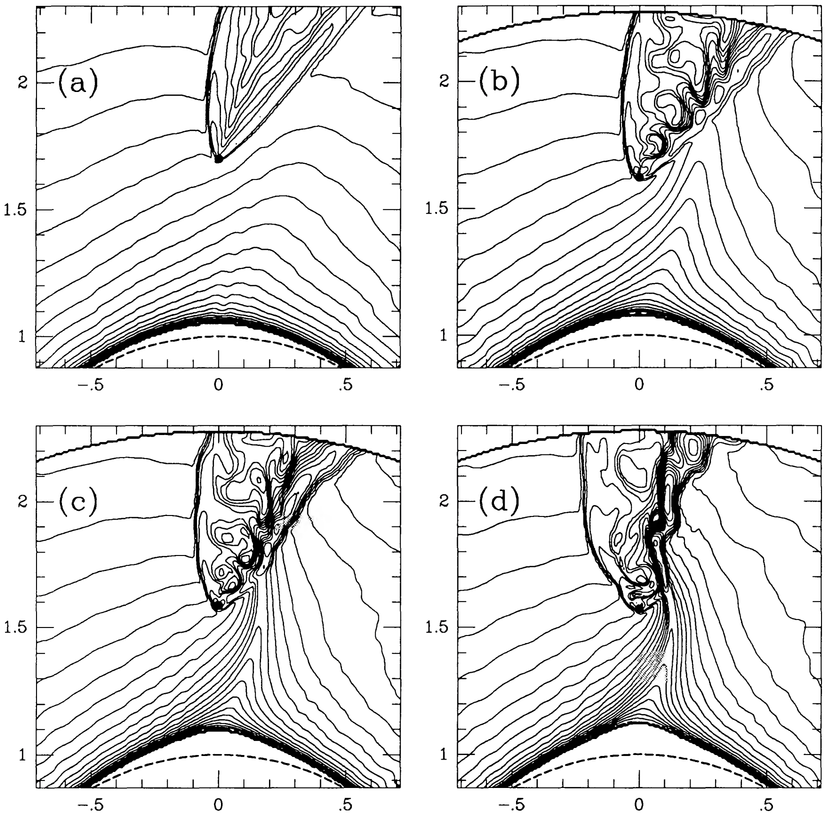

FIG. 1.—Formation of a gas stream as the binary separation is decreased in the MXRB models. The density contours are spaced logarithmically in units of $2^{1/2}$. The four plots are for different binary separations of $D/R_* = 1.70$ (*a*), 1.62 (*b*), 1.59 (*c*), and 1.57 (*d*). The physical dimensions of these plots are labeled in units of the stellar radius, $R_* = 2.45 \times 10^{12}$ cm, with the coordinate origin positioned at the center of the primary. The dashed line at the bottom of each plot marks the undistorted stellar surface of radius R_*.

---

[2] When the grid zoning is insufficient to resolve the accretion dynamics, e.g., an accretion disk, a tail shock is formed instead of a bow shock for this accretion problem.

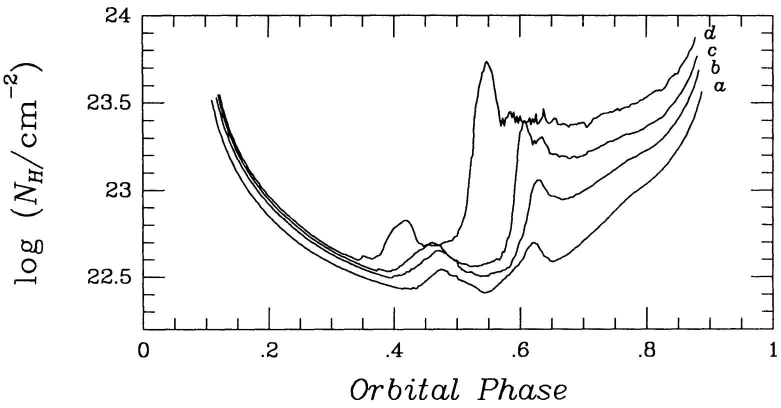

FIG. 2.—Line-of-sight column density as a function of orbital phase for the four models, *a–d*, shown in Fig. 1. Outside the numerical grid we assume that the wind density is that of an undisturbed wind, and thus may be underestimating N_H at some phases. The blank regions at early and late phases represent the eclipse of the X-ray source by the primary. While the contribution to N_H by the leading edge of the bow shock (around phases 0.4–0.5) remains relatively constant in the four models, the contribution by the tidal stream becomes very pronounced for small binary separation, extending from phase 0.5 all the way into eclipse.

Paper I; Fryxell & Taam 1988), leaving behind the "wavy" pattern seen in the accretion wakes of Figures 1*b*–1*d*. As the center of the gas stream joins the oscillating wake, it too is pushed around by the hot gas within the accretion wake. As the center of the gas stream approaches closer to the compact object, these oscillations become stronger and stronger, resulting in strong kinks in the stream once it has joined the accretion wake (Fig. 1*d*).

The large enhancement in the amount of material in the gas stream over that in the undisturbed wind will clearly have a major impact on the column density of material attenuating the X-rays from the compact object. In Figure 2 the variation of the absorbing column of material, N_H, is plotted as a function of orbital phase. The column density increases roughly monotonically with decreasing binary separation, with the highest values of N_H occurring for the model with $D/R_* = 1.57$. Each of the four model results plotted in Figure 2 shows a double-peaked structure, with one peak occurring slightly before phase $\Phi = 0.5$ and the second somewhat after. These two peaks correspond to the two sides of the accretion wake structure seen in Figures 1*a*–1*d*. In the model with $D/R_* = 1.70$, there is virtually no tidally enhanced gas stream and the two peaks in the column density are of similar magnitude. As the separation decreases, the magnitude of the tidally enhanced stream increases sharply, and because the gas stream tends to pass behind the compact companion, the column density of material after phase $\Phi = 0.5$ increases sharply, while comparatively little change is seen before $\Phi = 0.5$.

Although we have not been able to model a system with the photosphere at or above the critical Roche surface, the stellar surface of the primary in the last simulation in this series approaches within 1% of the Roche surface, and in fact the mass transfer to the compact companion is dominated by the dense wind flowing through the inner Lagrangian point, L_1. However, the mass loss along the line of centers is still dependent on the radiative acceleration to lift the material in the photosphere ultimately over the critical potential.

The sensitivity of the stellar wind to binary separation is also well illustrated in Figure 3, where the wind mass-loss rate is plotted as a function of azimuthal angle. At the smallest value of D/R_*, the mass-loss rate is an order of magnitude larger along the line of centers than the undisturbed wind for an identical, isolated O star. However, because the stream is relatively narrow, the mass loss within the stream is only a small fraction of the total mass loss from the star. For the strongest stream (Fig. 1*d*), the total mass-loss rate from the primary is increased only 9% by the contribution of the tidal stream.

In previous studies of this subject (e.g., Friend & Castor 1982; Stevens 1988) the enhanced mass-loss rate from the surface of the primary was assumed to lead to a correspondingly large enhancement of the mass accretion rate onto the compact star, $\dot{M}_{\rm acc}$. We have overcome this limitation by calculating the flow in two dimensions, which allows us to include orbital rotation along with the gravitational focusing in the orbital plane. We are still restricted to the flow in the orbital plane, however, and thereby neglect the gravitational focusing into this plane from above and below. We can, nonetheless, provide a much better estimate of the enhanced accretion rate caused by the formation of a tidal gas stream. In fact, we find that the center of the stream misses the neutron star as a result of deflection by the Coriolis force in all of our simulations (see Fig. 1). This is a result of the slow initial velocity of the wind relative to the orbital velocity, which allows the Coriolis force to deflect the wind strongly as it begins to accelerate off the

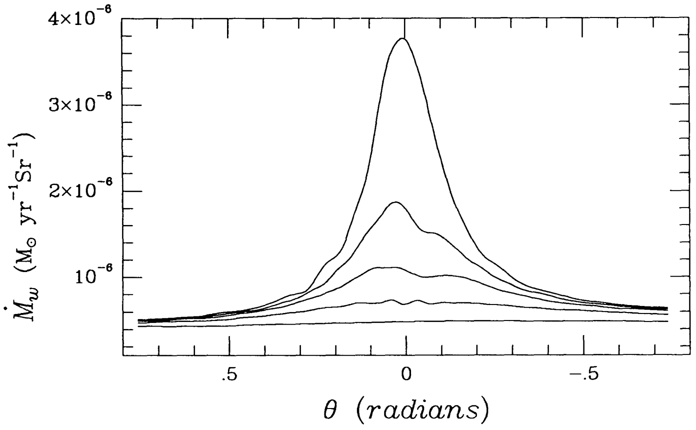

FIG. 3.—Angular dependence of the stellar wind mass-loss rate from the surface of the primary, calculated in the vicinity of the sonic point for each row of grid points in the radial direction. The angle θ is measured from the line of centers of the binary system. The five curves correspond to the binary separations of 1.57, 1.59, 1.62, 1.70, and 2.00, with the highest $\dot{M}_w$ corresponding to the smallest separation. The data have been smoothed with a running boxcar to remove the numerical noise associated with the imperfect boundary conditions (see discussion in § 2).

surface of the star. Thus, despite the fact that the density in the stream is ~30 times larger than the surrounding wind, we do not expect to see such a large increase in $\dot{M}_{\rm acc}$.

We have computed the mass accretion rate onto the compact object by calculating the mass flux across a circle of radius 10^{11} cm around the compact star. This radius is large enough to avoid the poorly resolved flow near the neutron star, and yet small enough to provide a reasonable estimate of the accreted mass (Paper I). In efffect this filters out the high-frequency "noise" in $\dot{M}_{\rm acc}(t)$. Note that because we are only calculating the flow in the equatorial plane, this calculation gives us a two-dimensional accretion rate in units of g $\rm s^{-1}$ $\rm cm^{-1}$ rather than g $\rm s^{-1}$, i.e., we are calculating the divergence of the flow within an accretion *circle* rather than an accretion *sphere*. To get a rough estimate of the total mass accretion rate, one should multiply the above two-dimensional rate by an appropriate accretion radius. Provided that the numerical zone size is less than the accretion radius (but not so much smaller that the accretion dynamics are well resolved: see § 3.2), the calculated accretion rate in numerical simulations with a spherical wind (no tidal distortion) agrees quite well with the dependence on separation given by the two-dimensional analog of the Bondi-Hoyle (1944) accretion rate of a gravitating body in a uniform flow. In this estimate, one assumes that all of the wind within an impact parameter given by the accretion radius, $r_{\rm acc} = \alpha G M_x / v_{\rm rel}^2$, is accreted onto the compact object (Davidson & Ostriker 1973). The resulting accretion rate is

$$\dot{M}_{\rm acc} \approx \frac{\alpha G M_x \dot{M}_w}{D^2 v_{\rm rel}^2}\,, \tag{2}$$

where $v_{\rm rel} = (v_w^2 + v_{\rm orb}^2)^{1/2}$ is the relative flow velocity at the compact object, $v_{\rm orb}$ is the orbital velocity of the compact object, and the radial wind velocity follows the relation $v_w = v_\infty(1 - R_*/r)^\beta$, with β typically ~0.8. A comparison of numerical simulations and this analytic estimate of $\dot{M}_{\rm acc}$ for a spherical primary suggests a value of $\alpha \approx 1.4$ for two-dimensional accretion of an adiabatic, $\gamma = 5/3$ gas. The good agreement with the Bondi-Hoyle rate is somewhat fortuitous, since the poor spatial resolution in the vicinity of the accreting star does not allow us to model the nonlinear dynamics of the accreting gas. In a sense, the poor resolution is smoothing out the flow, almost "forcing" the simple Bondi-Hoyle accretion flow. We will see in the next subsection that the accretion rate can be drastically different when the accretion dynamics are sufficiently resolved.

The increase in $\dot{M}_{\rm acc}$ provided by the gas stream is shown in Figure 4, where we compare the calculated $\dot{M}_{\rm acc}$ in the simulations with a distorted primary to the Bondi-Hoyle estimate for a comparable wind from a spherical primary (using $\alpha = 1.4$ as found above). The undisturbed wind for the simulations of Figure 1 is described by $\beta = 0.82$, $v_\infty = 1300$ km $\rm s^{-1}$, and $\dot{M}_w = 5.8 \times 10^{-6}\ M_\odot\ \rm yr^{-1}$. As illustrated in Figure 3, the mass accretion rate in the presence of a gas stream can be substantially higher than in the undisturbed case, with the enhancement in $\dot{M}_{\rm acc}$ increasing with smaller separation. At $D/R_* = 1.57$, the mass accretion rate is approximately 4 times higher owing to the contribution of the gas stream. As the binary separation increases, the distortion of the primary decreases and the mass accretion rate asymptotically approaches the Bondi-Hoyle estimate.

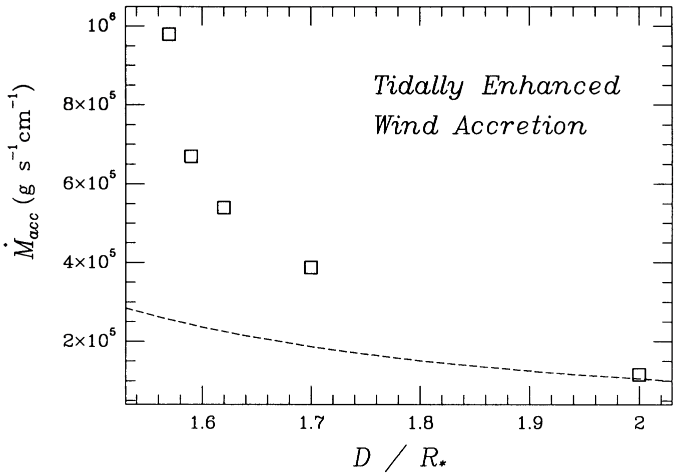

FIG. 4.—Dependence of mass accretion rate onto the compact object on the shape of the stellar surface. The open squares are the calculated values of the mass accretion rate in the series of simulations shown in Fig. 1. The dashed line is the Bondi-Hoyle estimate for the spherically symmetric case (eq. [2] in the text). The mass accretion rate is significantly enhanced at small binary separations due to the tidal distortion, and approaches the Bondi-Hoyle estimate at large separations.

Despite the fact that these simulations agree qualitatively with the higher resolution runs of Paper I, we caution that the resolution in these simulations is not sufficient to model the accretion flow accurately near the compact object. Thus, while the simulations of Figure 1 should provide a reasonable model of the gas stream leaving the star, the dynamics of the accretion wake and its interaction with the tidal stream may (and indeed is expected to) be different when modeled with higher spatial resolution. In addition, the gas stream may behave rather differently in the presence of an X-ray source, or may alter the effects of X-rays on the wind described in Paper I. In the following subsection we will investigate these effects using a higher resolution grid and the complete physics used in the models of Paper I.

3.2. *High-Resolution Runs*

Using the above prescription for modeling a corotating tidal bulge, we ran a "full" simulation incorporating all of the available physics described in Paper I. This allowed us to observe the interaction of the tidal bulge and gas stream on the heating, cooling, and X-ray ionization of the wind, and thereby derive a more complete description of the gas flow in MXRBs. In addition, we employed a higher spatial resolution in the vicinity of the compact object in order to provide a better model of the actual accretion flow dynamics. We used a numerical grid of 265 radial by 210 azimuthal zones, with the zone width at the compact object reduced to $\Delta R = 0.0015 R_*$. This spatial resolution is similar to that used in Paper I, and provides a more accurate simulation of the accretion dynamics. To separate the effects of the X-ray source from the effects of the higher spatial resolution, we first ran an adiabatic simulation as in the previous subsection, but on the high-resolution grid (Fig. 5). In this and the following full run we used a binary separation of $D = 1.59 R_*$, corresponding to the simulation shown in Figure 1c. We then ran the full simulation (Fig. 6) with an X-ray luminosity $L_x = 5.0 \times 10^{36}$ ergs $\rm s^{-1}$ and a critical ionization parameter log $\xi_{\rm cr} = 15$ (a value suggested by the work of Stevens & Kallman 1990).

The adiabatic model is shown in Figure 5 after several flow times. Aside from a lack of radiative cooling behind strong

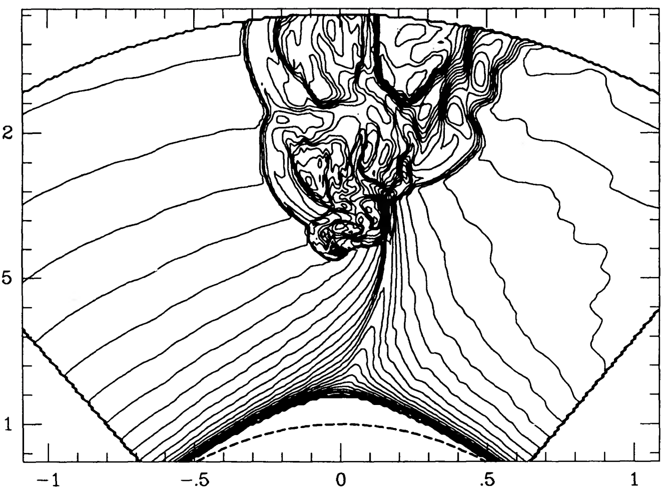

FIG. 5.—Tidal stream and accretion wake in the high-resolution, adiabatic simulation with parameters identical to the simulation depicted in Fig. 1*c*. The differences between this figure and Figure 1*c* are thus attributed solely to numerical resolution. Density contours are plotted at intervals of $2^{1/2}$. The smallest zone size (in the vicinity of the compact object) is ~ 5 times smaller than in the simulation of Fig. 1*c*. The decreased zone size allows a more accurate representation of the flow within the accretion bow shock, which in turn results in a larger and time-dependent accretion wake.

shocks, this simulation should resemble a low X-ray luminosity system. The only difference between this simulation and that of Figure 1*c* is the higher spatial resolution near the neutron star. While the gas stream appears similar in these two models, the bow shock and accretion wake of the high-resolution run are significantly larger and more complex. This is solely a result of resolving the accretion flow inside the accretion bow shock. As a consequence of resolving the bow shock oscillations, the accretion wake is both larger and more time-dependent, features we will discuss in more detail below.

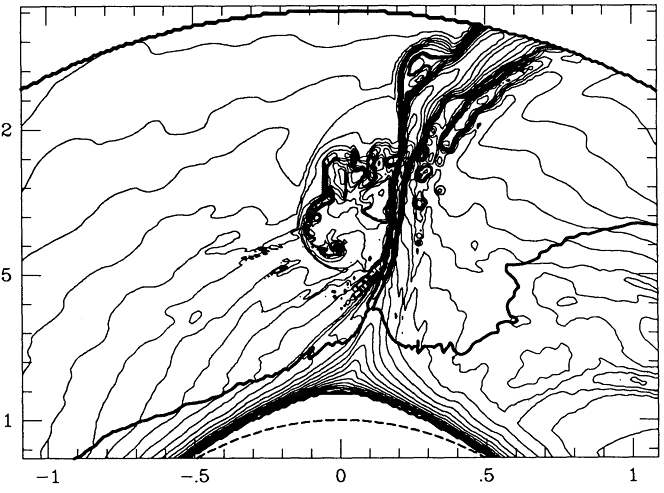

FIG. 6.—Tidal stream and accretion wake in the full model, including X-ray heating and photoionization and radiative cooling. Density contours are spaced a factor of $2^{1/2}$ apart. The model parameters are the same as those of Fig. 5, except for the X-ray luminosity $L_x = 5 \times 10^{36}$ ergs s^{-1}. The differences between this figure and Fig. 5 therefore represent the effects of the X-ray source on the wind. The heavy line marks the surface of the critical ionization parameter ($\log \xi_{cr} = 1.5$), beyond which the radiative force of the primary is cutoff. As a result of this cutoff, a weak photoionization wake can be seen at the extreme right-hand side of this plot (a gradual convergence of the density contours), where the unaffected wind collides with the photoionized wind.

In comparing this model with the simulations in Paper I, we find that the bow shock is relatively large compared with the corresponding simulation in Paper I (cf. Fig. 2 in Paper I). In fact, the flow shown in Figure 5 resembles the simulations of Paper I that include a photoionization cutoff, rather than the simulations with a fully accelerated wind. This is a result of the slower wind velocity in (and near) the gas stream, which leads to a relatively large accretion radius on the side of the compact star where the stream approaches, while the accretion radius on the other side is considerably smaller.

This strong asymmetry in the accreting wind drives an oscillation of the bow shock, similar to the behavior seen in the models of Paper I. After passing through the bow shock, the accreting gas converges in an accretion column that oscillates from side to side, producing "accretion disks" of alternating directions. In this particular simulation the flow is primarily counterclockwise (in the same direction as the orbit) near the neutron star, but circulates in the opposite sense for short periods of time. The temporal behavior is relatively uniform, with a period of ~ 3.2 hr.

The mass accretion rate reflects this quasi-periodic behavior, with an average accretion rate that is much lower than the value calculated in the model of Figure 1*c*. The average $\dot{M}_{acc}$ in this simulation is only $\approx 1.7 \times 10^{-5}$ g s^{-1} cm^{-1}, compared with the Bondi-Hoyle estimate of 2.4×10^{-5} g s^{-1} cm^{-1} for a comparable, undisturbed stellar wind. The instantaneous mass accretion rate reaches values of $\approx 3.9 \times 10^{-5}$ g s^{-1} cm^{-1}. The actual accretion rate onto the neutron star will depend critically on the formation and structure of an accretion disk from a radius of $\sim 10^{10}$ cm down to the stellar surface (or magnetosphere). This lower $\dot{M}_{acc}$ in our model is the result of the formation of an accretion column with large angular momentum, as seen in many of the simulations of Paper I. In this configuration most of the post–bow-shock flow approaches the compact object along an accretion column that swings the flow around the side of the star facing the primary and terminates in a strong spiral shock. The gas flowing in along this column possesses too much angular momentum to approach the neutron star any closer, forming an effective angular momentum barrier. While the presence of spiral shocks in the disk allows the accretion of some disk mass, only a small fraction of the infalling gas will be accreted, with the remainder being swept downstream with the accretion wake. Although the amount of matter accreted through the disk in a simulation such as this will depend on the numerical resolution of the spiral shocks in the disk, the accretion rate is expected to remain significantly lower than in the absence of a disk. This lower $\dot{M}_{acc}$ is different from the oscillating-disk case (e.g., Fryxell & Taam 1988), where large dumps onto the compact object during disk reversal substantially increase the average mass accretion rate. The large asymmetry of the accreting wind in this problem results in less frequent disk reversals and hence lower average $\dot{M}_{acc}$.

The presence of an X-ray source will strongly affect the accretion flow described in the above simulation through both heating and cooling, and through photoionization, which decreases the radiative force exerted by the primary (Paper I). The sum of these effects can be seen by comparing Figures 5 and 6, which differ only in the presence of a strong X-ray source in Figure 6. The influence of the X-ray photoionization is evident both in the size of the bow shock and in the discontinuity in the wind near the surface of the primary. Because of the slower wind at the compact object, the accretion radius is

1991ApJ...371..684B

significantly larger in this similation compared with that of Figure 5. In fact the bow shock stands $\sim 2 \times 10^{11}$ cm off the compact star, significantly more than in any of the simulations of Paper I. The location of the surface $\xi = \xi_{\rm cr}$ is seen to coincide with a clear discontinuity in the wind, illustrating the strong effect of removing the wind acceleration. Although the effects of X-ray ionization may not be as abrupt in real systems, the wind velocity is still expected to be drastically reduced in the vicinity of the compact object.

Despite the obvious influence of photoionization on the wind velocity, there is only a very weak photoionization wake trailing the compact star. This is in contrast to the simulations of Paper I with similar values of the mean wind ionization parameter, $q_i \propto \dot{M}_w/L_x$ (see Paper I for a complete definition of q_i), which exhibit very strong photoionization wakes for q_i less than a few ($q_i \approx 1$ in this run). The difference is directly attributed to the presence of the tidal stream. The material that forms the stream leaves the primary at a closer distance to the X-ray source, and is moving much slower than the wind from an undistorted primary. Both of these effects result in a stream that is strongly deflected by the gravitational potential of the compact star. This results in less wind material trailing behind the compact star in its orbit, and hence less material that can be compressed by the undisturbed stellar wind, producing a photoionization wake. On the basis of these simulations, it appears that the tidal stream and the photoionization wake are largely exclusive.

Another difference in the full simulation compared with the adiabatic run is the relatively narrow accretion wake downstream, and the thin, dense filaments therein. This is the result of short cooling times brought on by the high densities in the vicinity of the tidal stream. Although the center of the stream misses the compact star, the wind striking the apex of the accretion bow shock is still a few times denser than it would be without a tidally distorted primary. This high density leads to rapid cooling behind the bow shock, which forms a thin layer of dense gas, as in a typical radiative shock in the interstellar medium (e.g., an old supernova remnant). The tidal stream also remains relatively narrow after colliding with the accretion wake, as the radiative energy losses keep the stream cold.

An example of the typical structure of these filaments in the vicinity of the neutron star is given in Figure 7. The narrow tidal stream is visible on the right-hand side of the plot, while a narrow filament roughly parallel to the bow shock can be seen on the left-hand side of the neutron star. While this dense postshock layer eventually coalesces with the tidal stream downwind of the neutron star, it is occasionally disrupted via dynamical instabilities, forming separate clumps of dense gas. Several such clumps can be seen in Figure 7, with densities comparable to that of the tidal stream. These clumps are formed when the hot, rarefied gas that is accelerated around the neutron star pushes on the cold, dense gas forming behind the bow shock, When the momentum flux in the hot flow becomes sufficient to accelerate the denser gas, the filaments become Rayleigh-Taylor–unstable. In our simulations the postshock layer quickly breaks up into separate clumps, some of which are advected downwind and some of which are eventually accreted. From the time sequence of the full simulation, it appears that it is the (partial) accretion of one of these clumps that increases the momentum flux of the gas coming around the neutron star, which in turn drives the Rayleigh-Taylor instability to form new clumps.

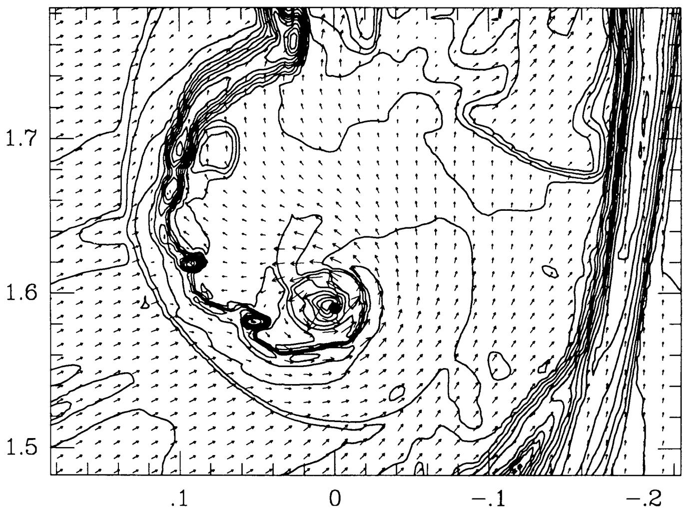

FIG. 7.—Expanded view of the gas flow within the accretion bow shock for the simulation shown in Fig. 6. The compact object is marked by the solid dot in the center of the plot. This dot is roughly twice as large as the numerical boundary representing the compact object. The density contours are spaced in logarithmic increments of 1.5. The velocity vectors are scaled linearly, with the largest vector representing a velocity of 1.4×10^8 cm s^{-1}. The bow shock is seen along the left and bottom of the plot as an increase in density and as a discontinuous decrease in velocity. The maximum Mach number of the bow shock is ~ 1.9. The tidal stream flows along the right-hand side of this plot. Rayleigh-Taylor "clumps" are visible to the left of the compact object. These clumps are created as the gas flowing away from the compact object pushes on the dense gas that has cooled behind the bow shock. The roughly circular contours near the compact object mark the region of rarefied gas inside the angular momentum barrier. The gas in this region is orbiting with roughly Keplerian velocity.

Another effect of the tidal stream/bow shock interaction is the continuous rotation of the accreting gas around the compact object in the same direction. This flow pattern is illustrated in Figure 7. The close proximity of the stream to the bow shock effectively locks the accretion column to the leading side of the compact star. The accreting specific angular momentum remains positive (in the same sense as the orbit) for the bulk of the simulation. This can also be thought of as a very large asymmetry in the accreting wind caused by the presence of the tidal stream (Fryxell & Taam 1988). The mass accretion rate, although relatively low, is occasionally augmented by the accretion of one of the Rayleigh-Taylor clumps created behind the bow shock. These accretion events could produce bursts of X-rays more than a magnitude larger than the quiescent X-ray luminosity, and on time scales of several minutes to an hour.

The high densities in the accretion wake/tidal stream caused by strong radiative cooling suggest that there will be strong attenuation of soft X-rays when the system is observed near phase 0.6. The photoionization wake, on the other hand, is barely noticeable, and does not produce significant absorption of X-rays at late phases. The phase dependence of the absorption column density is shown in Figure 8. The separate clumps of dense gas seen near the compact object in Figure 7 produce distinct peaks in $N_{\rm H}(\Phi)$ around phase 0.3–0.5. These peaks will vary on time scales comparable to $r_{\rm acc}/v_{\rm ff}(r_{\rm acc})$, or about 3 hr in this model. This time corresponds to less than 2% of the orbital period, implying that some of the structure seen in the inferred $N_{\rm H}$ will be determined by gas motion within the accretion wake rather than by orbital motion changing the line of sight. Note that the column density of the undisturbed wind (*dotted line*) is usually well below the computed column density in the model, suggesting that any attempt to interpret the

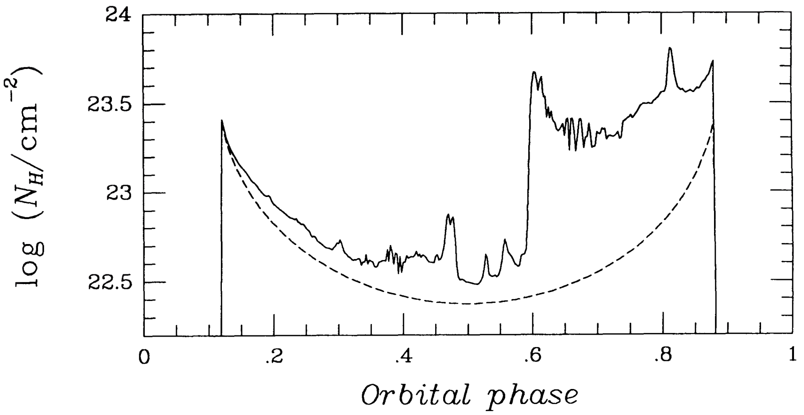

FIG. 8.—Line-of-sight column density as a function of orbital phase. The solid line is the integrated line-of-sight column density from the full simulation at the same time as shown in Figs. 6 and 7. Outside the numerical grid we assume that the wind density is that of an undisturbed wind, and thus may be underestimating N_H at some phases. The dotted line marks the column density of the undisturbed wind from a spherical primary. The blank regions at early and late phases represent the eclipse of the X-ray source by the primary. The individual clumps seen in Fig. 7 are visible as small peaks in N_H around phases 0.3–0.5.

"baseline" of undisturbed wind from observations of $N_H(\Phi)$ could result in an overestimate (cf. Haberl et al. 1989). This reflects the fact that, for a strong X-ray source, a large region of the wind is disturbed and the inferred N_H to the X-ray source is affected at all observed orbital phases.

4. DISCUSSION

The simulations described in this paper illustrate several important points regarding stellar wind accretion in MXRBs. The four adiabatic simulations in Figure 1 show graphically that the assumption of spherically symmetric mass loss and RLOF are merely the two asymptotic extremes of one physical process at work in MXRB-type systems, there being a continuous spectrum of variation from one to the other as the stellar separation changes. These models also demonstrate the sensitivity of the strength of the tidal stream to the stellar separation, or more particularly to the ratio D/R_*. A 10% reduction in D/R_* can produce a tidal stream many times as dense. The sensitive dependence of the tidal stream on stellar parameters provides a potential diagnostic for the stellar and orbital parameters in such systems as Vela X-1 and 4U 1700−37. Through observations of the X-ray attenuation at different orbital phases, one can infer the presence or absence of a tidal stream, which can, in turn, constrain the size of the primary with respect to its Roche lobe.

The low-resolution models of § 3.1 showed an increase in $\dot{M}_{\mathrm{acc}}$ over the Bondi-Hoyle estimate for decreasing binary separation. Although we do not have the same data available for the higher resolution models, we might expect this behavior to remain at higher numerical resolution. However, the change in the accretion dynamics brought about by the tidal stream may alter this conclusion. An indirect comparison of the simulation in Figure 6 with the models of Paper I suggests a small (factor of ~ 1.4) increase in $\dot{M}_{\mathrm{acc}}$ attributable to the tidal stream.

When compared with the results of Paper I, the models presented in this paper, in which the primary is close to its Roche lobe, show the following effects on some of the observable properties of MXRBs: a reduction or absence of changes in the sign of the net angular momentum of the accreted material, and hence in the sign of the spin period derivative of a neutron star in such a system; an absence of the "photoionization wake" first suggested to occur by Fransson & Fabian (1980), which was shown in Paper I to occur preferentially in systems where the wind is more highly ionized, i.e., when the ratio of $L_x/\dot{M}_w$ is greatest; and greater X-ray absorbing columns at orbital phases 0.5 and later.

4.1. *Comparison with Observations*

The five best-studied MXRBs have a range of observed properties which allow us to test some of the predictions of these models and those of Paper I. These properties include the stellar radii (as inferred from the spectral classification), the Roche or tidal lobe radius inferred from the orbital elements, the mean ionization of the wind (q_i, based on observationally derived L_x and $\dot{M}_w$), the mass accretion rate onto the compact object as inferred from L_x, the X-ray variability (on time scales of hours to days), the spin period history (available only for the best-studied pulsars), and the X-ray absorption as a function of orbital phase.

Estimates for the stellar radii and critical (Roche or tidal) radii have been tabulated by Conti (1978), who showed that the primaries of all the known systems are near to overflowing their critical lobes, and that the uncertainties in estimating these quantities is great enough to prevent any classification of the sources based on these quantities. Another test for the effects of overflow is the comparison of the mass accretion rate onto the compact object required to power the observed X-rays with that expected from Bondi-Hoyle theory (Davidson & Ostriker 1973). Such a comparison shows that only two of the systems, Vela X-1 (4U 0900−40) and 4U 1700−37, are capable of sustaining their observed mass accretion rates from wind accretion alone (Conti 1978; Petterson 1978). Furthermore, recent UV spectroscopy of these systems by Corcoran & Heap (1990) and Heap & Corcoran (1990) has resulted in downward revision of the stellar radii and masses for both these systems relative to those used in the past. On the other hand, estimates of the wind-supplied mass accretion rate are very sensitive to the wind properties (velocity and mass-loss rate), and we cannot rule out the possibility that these objects have tidal streams together with winds somewhat weaker (or faster) than had been previously thought.

The phase-dependent absorption of X-rays affords a more detailed look at the gas flow within the binary system. In Paper I we showed that, in the absence of tidal effects, the structures that dominated the accretion flow near the compact object are either an accretion "bow shock" which occurs preferentially at low to intermediate values of the ratio $L_x/\dot{M}_w$ and which is highly variable in time but does not produce significant absorption at late orbital phases, or a "photoionization wake" at large $L_x/\dot{M}_w$ which is relatively steady in time but can produce strong absorption at late phases. This paper describes a third structure, the tidal stream, that is also steady in time and produces absorption from phase ~0.5 all the way into eclipse. The models in this paper suggest that when tidal effects are important, the structures resembling the photoionization wake never form, even for large values of $L_x/\dot{M}_w$. Thus systems which show strong, relatively orbit-independent absorption at late phases must either have large $L_x/\dot{M}_w$ or primary stars which are near their critical surface. Conversely, a lack of strong attenuation around phases 0.6–0.7 would imply both the lack of a significant tidal stream and a low to moderate ratio of $L_x/\dot{M}_w$.

Detailed observations allowing the inference of the absorbing column as a function of orbital phase have been made for the two systems in which critical lobe overflow is not needed to explain the accretion rate, Vela X-1 (4U 0900−40) and 4U 1700−37. Vela X-1 was observed by *EXOSAT* (Haberl 1989) over several different orbits, which, when taken together, cover the major portion of one complete orbital cycle, although significant gaps still exist. These observations and the *Copernicus* data reported on by Charles et al. (1978) show a general trend of higher column densities at later phases. Haberl interprets these data as showing two components: a base level that is reproducible from orbit to orbit and gradually increases an order of magnitude toward late phases, and a highly variable component with peaks an order of magnitude above the base level, occurring primarily at late phases. In addition, one of the narrow peaks is reproduced in more than one orbit, and sits right at phase 0.5. This interpretation by Haberl agrees qualitatively with our model of an MXRB with a moderate tidal stream (compare Fig. 6 of Haberl 1989 with our Fig. 2). The gradually increasing base component at $\Phi > 0.5$ is the attenuation of the time-independent tidal stream. An examination of our models suggests that the large peak at $\Phi = 0.5$ may represent the line of sight looking down the length of the tidal stream downstream from the neutron star. This association of the absorption peak with the tidal stream implies that this particular peak in column density will be reproducible from orbit to orbit, as the tidal stream remains relatively time-independent.

Also of interest is the fact that the *EXOSAT* observations of Vela X-1 do seem to show distinct peaks in the value of $N_{\rm H}$ not associated with eclipse ingress or egress. These peaks are seen at almost every phase, and are generally not reproduced from orbit to orbit. While the location of these absorption peaks is not exactly the same as those predicted in Figure 8, it is possible that the observations are revealing density structures associated with the accretion wake, the bow shock, or the tidally enhanced stream. By analogy with the separate peaks visible in Figure 8 at phases 0.3–0.6, the observed peaks in the *EXOSAT* data may be produced by separate clumps formed by dynamical instabilities inside the accretion bow shock. In comparing our Figures 2 and 8 with the *EXOSAT* observations, it is clear that we have overestimated the density in the undisturbed wind. This is due to our derived terminal velocity of 1300 km s^{-1}, compared with the observed value of ~1700 km s^{-1} (Conti 1978) and a wind mass-loss rate a factor of 3 less than that suggested by Conti. Although the lower density will change the heating and cooling rates, the tidal stream will not be affected.

The phase variability of the absorbing column in 4U 1700−37 as observed by *EXOSAT* is reported by Haberl et al. (1989). These observations cover a large fraction of one complete orbit cycle (with a significant gap in their coverage at late phases). These observations suggest, as do the *Copernicus* observations reported on by Mason, Branduardi, & Sanford (1976), a significantly higher level of attenuation after phase $\Phi = 0.5$ than before, in qualitative agreement with the models shown in Figure 2. In particular, the *EXOSAT* observations show a sharp rise just after $\Phi \approx 0.6$, and a large excess at $\Phi \approx 0.8$ (near eclipse ingress). Unfortunately, these observations do not provide coverage over the important phase range of 0.7–0.8, making any direct comparisons with models rather tentative. If this excess absorption were caused by a tidal stream, one would observe strong attenuation from phase 0.6 all the way into eclipse on every orbit. The current observations may also be explained by an accretion wake, which would imply that the absorption features seen by *EXOSAT* will be significantly different in subsequent observations, and need not remain high through the gap from phase 0.7 to phase 0.8. This object has the lowest inferred $L_x/\dot{M}_w$ ratio of any of the observed MXRBs, making it an unlikely candidate for a photoionization wake.

In spite of the apparent consistency between the observed X-ray absorption as a function of orbital phase and that predicted by our models, it is important to note that models such as those presented in Figure 6 have a rather different variability behavior than models without a tidal stream, as in Paper I. In particular, models with a significant tidal stream show weak or absent changes in the sign of the accreted angular momentum, $\dot{J}$. Since this quantity is expected to be directly correlated with changes in pulsar spin period in MXRBs such as Vela X-1, the spin period history of these systems provides an important constraint on our models. For Vela X-1, studies of the pulsar $\dot{P}$ over a 10 yr period have been shown to be consistent with a stochastic variation in the accreted $\dot{J}$, with changes in the sign of $\dot{P}$ occurring on the shortest observed time scales of 2 or 3 days (Deeter et al. 1989). These frequent changes in the sign of $\dot{P}$ on short time scales agree well with the models of Paper I, but they are inconsistent with the models of this paper possessing a dominant tidal stream.

The observed pulsar spin history of Vela X-1 thus suggests that there is no significant tidal stream, contradicting our conclusion made above based on the observed $N_{\rm H}(\Phi)$. We note, however, that the observations suggest only a moderate tidal stream, since the enhanced absorption around phase 0.6 is lower than that at later phases. While we have not modeled a moderate stream at high resolution, it may be possible that oscillations in $\dot{J}$ may still occur for a mildly distorted wind as in Figure 1*b*. On the other hand, our models may simply be insufficient to model the true time variability in $\dot{J}$. Possible influences on $\dot{J}$ include unresolved gasdynamics near the compact object, interaction between an accretion disk and the compact object, or effects limited to three dimensions.

The other three systems listed in Conti (1978), Cen X-3, SMC X-1, and Cyg X-1 are more likely to possess a tidal stream, since their X-ray luminosities are higher than that expected from undisturbed wind accretion alone. Although Ho & Arons (1987) claim that an X-ray–ionized wind can increase the mass accretion in these systems to explain their high luminosity, we found a more modest increase in $\dot{M}_{\rm acc}$ due to this effect (roughly an order of magnitude; Paper I), insufficient to explain the observed L_x. The ellipsoidal light variations in these systems imply that the primaries are significantly distorted (Avni & Bahcall 1975), supporting the role of a tidal stream or RLOF. Indirect evidence also comes from the relatively constant pulsar $\dot{P}$ observed in Cen X-3 and SMC X-1 (Cyg X-1 is a black hole candidate and does not exhibit regular pulsations), which suggests the presence of a disk or tidal stream to maintain a $\dot{J}$ of unique sign (Joss & Rappaport 1984). Note that our models demonstrate that a relatively constant $\dot{P}$ can be explained by a tidal stream alone, without resorting to a true accretion disk. In addition, van Paradijis & Zuiderwijk (1977) claim evidence for an accretion disk in the observed optical light curves of SMC X-1.

Cen X-3 exhibits strong absorption from phase 0.5 to phase 0.75 when in the high-luminosity state (Pounds et al. 1975). While these data are not as detailed as the *EXOSAT* data for Vela X-1 and 4U 1700−37, the drop in X-ray luminosity is very pronounced and remains for several orbits, consistent with our models of tidal streams. SMC X-1, on the other hand, does not show strong phase-dependent absorption (Marshall, White, & Becker 1983). This may be a result of the only moderately high inclination of 64°–70° implied by the relatively short eclipse (Hutchings et al. 1977), although such an explanation would only avoid the attenuation of the tidal stream and not an accretion wake or photoionization wake, since the latter two will occur out of the orbital plane as well. However, the absence of phase-dependent absorption may not be surprising. First of all, it may have only a very weak wind, consistent with its spectral type and the wind properties of other SMC stars (Hammerschlag-Hensberge, Kallman, & Howarth 1984). Second, SMC X-1 has by far the smallest value of q_i (highest mean wind ionization) in this sample of MXRBs. Thus, the X-ray flux may ionize the stellar wind near the surface of the primary to suppress the wind radiative driving, resulting in an even smaller mass-loss rate from the side of the primary exposed to the X-ray flux.

There is evidence for phase-dependent absorption in Cyg X-1, although the strongest attenuation events have occurred at phase 0, i.e., when the X-ray source is behind the primary. This system shows no eclipse, with an estimated inclination of 30°–40° (Bolton 1975). The column density of these attenuation events is typically $(2\text{–}3) \times 10^{22}$ cm^{-2}. Although the X-ray luminosity is sufficiently low to be driven by the stellar wind alone (at least in the low-luminosity state; Petterson 1978; Ho & Arons 1987), He II emission-line data at least hint at the presence of a tidal stream (Hutchings et al. 1973).

4.2. *Departures from Corotation*

The models presented in § 3 have all been calculated assuming corotation, whereby the stellar rotational angular velocity Ω is equal to the binary angular velocity ω. In this case, as shown in Figures 1, 5, and 6, the tidal bulge lies on the line of centers of the system. However, in those MXRBs for which reasonably reliable data are available, significant departures from corotation are inferred. For example, Cyg X-1 and SMC X-1 are thought to corotate, while 4U 1700−37, Cen X-3, and Vela X-1 are all believed to rotate slower than required for synchronicity (Conti 1978).

Only in the situation of a binary system where the orbit is circular, and the primary stellar rotation is aligned and synchronized with the binary period, will the tidal deformation be hydrostatic. Any departures, such as a nonsynchronized rotation, as in the case of Vela X-1, or an eccentric orbit (Vela X-1 also seems to have a small eccentricity, although this too has been ignored in the calculations presented above; Joss & Rappaport 1984), will result in the primary experiencing a time-dependent potential.

Zahn (1975) has calculated the effects of nonsynchronous rotation on tidal evolution in close binary systems, and found that the equilibrium tidal bulge is typically an order of magnitude larger than the time-dependent dynamical bulge. Only at the peak of a resonance will the dynamical bulge be comparable in size to the equilibrium bulge. Thus, the approximation that we have used of calculating the tidal bulge in the hydrostatic approximation will be not unreasonable, with significant departures from this situation occurring only for short intervals as the system passes through a resonance. However, the angular momentum of the wind leaving the primary's surface will be lower for stars spinning at less than corotation, and any tidal stream will be deflected further behind the compact object in orbit. Furthermore, the time dependence of the dynamical bulge could result in highly variable mass loss. This complicated dynamical problem should be considered in greater detail, especially given that most MXRBs are inferred to rotate slower than needed for synchronization.

As a final note, the full numerical simulations presented in § 3.2 were calculated assuming a constant X-ray luminosity. The observations of MXRBs and the calculation of the mass accretion rate in these simulations show that the X-ray luminosity will vary on relatively short time scales, showing strong flares and dips. The inclusion of the feedback effects of this nonsteady X-ray behavior on the wind dynamics remains a further significant improvement that should be included in future models, and should add greatly to our understanding of the temporal behavior of MXRBs.

5. SUMMARY

In this paper we have presented further simulations of the two-dimensional gasdynamics in MXRB systems, including the effects on the wind dynamics of such mechanisms as X-ray ionization and heating. The major improvement in this work over that of Paper I is the inclusion of the tidal distortion of the primary star and the resultant changes in the wind dynamics. We find that this tidal distortion gives rise to a stream of enhanced stellar wind in the direction of the compact companion. This tidal stream is expected to evolve into Roche lobe overflow as the surface of the primary star approaches its critical potential surface. The additional mass loss associated with the tidal stream, while not being a significant perturbation of the total mass loss from the primary star, has a very strong influence on accretion structures formed close to the neutron star, as well as on the amount of attenuating material within the binary system. These models suggest that MXRB systems with a dominant tidal stream will show strong X-ray attenuation from orbital phase ~0.6 into eclipse (for low orbital inclination), a modest increase in the X-ray luminosity over that predicted by the simple Bondi-Hoyle theory, and a constant sign in the derivative of the rotational period.

In the process of studying these models, we have constructed "movies" by displaying the flow at successive time steps. The time-dependent behavior exhibited by our models is best seen in these movies. Videotapes of the simulations described in this paper and in Paper I are available directly from the authors.

We thank the referee, Bruce Fryxell, for his insightful, timely comments. This work was supported in part by the National Science Foundation under grant AST-8818362. The numerical simulations were computed on the Cray X-MP/48 at the National Center for Supercomputing Applications at the University of Illinois at Urbana-Champaign.

REFERENCES

Avni, Y., & Bahcall, J. N. 1975, ApJ, 197, 675

Blondin, J. M., Kallman, T. R., Fryxell, B. A., & Taam, R. E. 1990, ApJ, 356, 591 (Paper I)

Bolton, C. T. 1975, ApJ, 200, 269

Bondi, H., & Hoyle, F. 1944, MNRAS, 104, 273

Castor, J. I., Abbott, D. C., & Klein, R. I. 1975, ApJ, 195, 157 (CAK)

Charles, P. A., Mason, K. O., White, N. E., Culhane, J. L., Sanford, P. W., & Moffatt, A. F. J. 1978, MNRAS, 183, 813

Collela, P., & Woodward, P. R. 1984, J. Comp. Phys., 54, 174

Conti, P. S. 1978, A&A, 63, 225

Corcoran, M., & Heap, S. 1990, ApJ, submitted

Davidson, K., & Ostriker, J. P. 1973, ApJ, 179, 588

Deeter, J. E., Boyton, P. E., Lamb, F. K., & Zylstra, G. 1989, ApJ, 336, 376

Eadie, G., Peacock, A., Pounds, K. A., Watson, M., Jackson, J. C., & Hunt, R. 1975, MNRAS, 172, 35P

Fahlman, G. G., & Walker, G. A. H. 1980, ApJ, 240, 169

Fransson, C., & Fabian, A. C. 1980, A&A, 87, 102

Friend, D. B., & Abbott, D. C. 1986, ApJ, 311, 701

Friend, D. B., & Castor, J. I. 1982, ApJ, 261, 293

Fryxell, B. A., & Taam, R. E. 1988, ApJ, 335, 862

Fryxell, B. A., Taam, R. E., & McMillan, S. L. 1987, ApJ, 315, 536

Haberl, F. 1989, Two Topics in X-Ray Astronomy, ed. N. White (ESA SP-296), 31

Haberl, F., White, N. E., & Kallman, T. R. 1989, ApJ, 343, 409

Hammerschlag-Hensberge, G., Kallman, T. R., & Howarth, I. D. 1984, ApJ, 283, 249

Heap, S., & Corcoran, M. 1990, ApJ, submitted

Ho, C., & Arons, J. 1987, ApJ, 316, 283

Hutchings, J. B., Crampton, D., Cowley, A. P., & Osmer, P. 1977, ApJ, 217, 186

Hutchings, J. B., Crampton, D., Glaspey, J., & Walker, G. A. H. 1973, ApJ, 182, 549

Joss, P. C., & Rappaport, S. A. 1984, ARA&A, 22, 537

Kallman, T. R., & White, N. E. 1982, ApJ, 261, L35

Kruszewski, A. 1963, Acta Astr., 13, 106

Lubow, S. H., & Shu, F. H. 1975, ApJ, 198, 383

Marshall, F. E., White, N. E., & Becker, R. H. 1983, ApJ, 266, 814

Mason, K. O., Branduardi, G., & Sanford, P. 1976, ApJ, 203, L29

Pauldrach, A., Puls, J., & Kudritzki, R. P. 1986, A&A, 164, 86

Petterson, J. A. 1978, ApJ, 224, 625

Pounds, K. A., Cooke, B. A., Ricketts, M. J., Turner, M. J., & Elvis, M. J. 1975, MNRAS, 172, 473

Stevens, I. R. 1988, MNRAS, 232, 199

Stevens, I. R., & Kallman, T. R. 1990, ApJ, 365, 321

Tassoul, J.-L. 1978, Theory of Rotating Stars (Princeton: Princeton Univ. Press)

van Paradijs, J., & Zuiderwijk, E. 1977, A&A, 61, L19

Zahn, J.-P. 1975, A&A, 41, 329